Doppler line shape model for the W I 5d 5 6s-5d 5 6p transition at 400.9 nm in tokamaks

A Sepetys, R Guirlet, J Rosato, Y Marandet

Doppler line shape model for the W I $5d^5 6s$ - $5d^5 6p$ transition at 400.9 nm in tokamaks

A. Sepetys [1], R. Guirlet [1], J. Rosato [2], Y. Marandet [2]

[1] CEA - IRFM, Cadarache, 13108 – Saint-Paul-lez-Durance, France

[2] Aix-Marseille Univ., CNRS, PIIM, Marseille, 13397 Cedex 20, France

Abstract. Tungsten spectroscopy is known to be a useful tool for quantifying W fluxes in tokamaks. We aim to analyze how background plasma parameters influence the W spectral-line shape measured in the divertor and scrape-off layer and what information could be retrieved from such an analysis. To that end, a Monte Carlo model is developed to simulate the line shape of the 400.9 nm W I line emitted by physically sputtered W ions from plasma facing components. The influence of background plasma parameters (ion and electron temperature) and geometrical effects (detector positioning with respect to the eroded surface) are investigated. The effect of Zeeman splitting on the spectral line-shape is also explored. A set of requirements for the experimental set-up needed to measure the analyzed spectral line features with line peak shifts of the order of 10^{-2}Å and peak widths in the range from 10^{-1}Å to 10^{-2}Å are proposed. These requirements are shown to be experimentally accessible, through the installation of specific high-resolution spectrometers not typically used on magnetic fusion devices.

Keywords: Tungsten, sputtering, fusion, line-shape, Zeeman

1. Introduction

For a long time a favored material for plasma facing components in fusion reactors was carbon. However due to its high hydrogen retention and high erosion rate it was deemed unfit for new generation fusion reactors. This has propelled a research into application of high Z materials in fusion reactors, due to their lower erosion and capability to handle high heat loads.

Tungsten was found to have the desired thermo-mechanical properties as well as low tritium retention. For these reasons ITER will be equipped with a W divertor and an increasing number of tokamaks are already running with partial or complete W walls (ASDEX-Upgrade [1], JET [2] and now WEST [3]). However, tungsten is a high Z material and can lead to high radiation losses and eventually to a complete loss of confinement, if its content within the plasma is not controlled [4, 5].

One aspect of W content control is the characterisation of its sources within the tokamak. The primary tungsten source is expected to be a neutral particle flux from the plasma facing components originating from their physical erosion. The local neutral W flux can be inferred spectroscopically from a W I line and the so called S/XB factor [6, 7]. It is also well known that parameters such as the density and temperature of the emitting population can usually be inferred from the spectral line shape [8, 9, 10, 11].

It is expected that the shape of tungsten low ionization stage spectral lines can help to characterize W sources by providing information about the neutral W velocity distribution. This comes from the Doppler effect as the wavelength for the transition changes due to motion of the source atoms. The resulting Doppler line profile should in principle reflect key aspects of sputtering physics (e.g. energy and angular distribution of sputtered atoms) and be sensitive to the energy of ions responsible for sputtering. However, as tungsten atoms have a large atomic mass, the velocities of sputtered particles are low, which results in a small Doppler shift. It is thus expected that accessing this information will require specific very high-resolution spectrometers, and one of the aims of this work is to quantify these requirements. To study this wavelength change a Monte Carlo based model was developed to estimate the Doppler profiles of neutral W lines. The model includes the physical sputtering process of the target material, the Doppler shift of the photons emitted by the sputtered atoms. Obtaining line profiles further requires accounting for the Zeeman effect, which is line dependent. In this work we apply the model to the case of the most commonly observed W I line at 400.9 nm [6, 12], since this allows to discuss the main parameters determining the line shape and the instrumental requirements to analyse these line profiles. Applying the analysis to several W I lines simultaneously would allow to check the consistency of the measurements with the calculated Zeeman profiles and identify possible parasitic line contributions to the W I lines, and is thus highly recommended. Furthermore, the analysis could also be coupled to W II line measurements in order to further strengthen the results and evidence the degree of thermalization of W II ions.

The outline of the paper is as follows: the model for the Doppler line shape is discussed in section 2, and the results are presented in section 3 for a set of relevant projectiles and plasma conditions. The Zeeman effect resulting from the confining magnetic field is discussed in section 4. The results are then summarized in section 5, where an assessment of the information potentially retrievable from a W I line shape analysis is presented, together with the experimental requirements.

2. W atom source and emission

The model for the sputtered ion velocity distribution to be presented in this section is schematically represented in Figure 1. The W source process is assumed to be the sputtering of W atoms by an ion flux accelerated in the magnetized sheath and hitting a planar W surface representing a divertor plate or a limiter.

We aim to estimate the sputtered tungsten atom velocity distribution arising from the incoming ion flux characteristics and sputtering properties of the W target. From the velocity distribution thus derived and geometrical features of the experimental setup

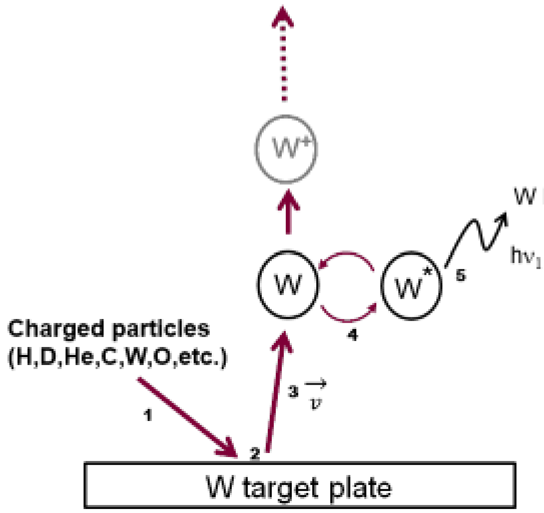

Figure 1. Schematic representation of the model (see text for description)

we calculate the spectral line shape. The analysis discussed here is aimed at neutral W spectral line emission which can only occur at a very narrow layer within the scrape off layer (SOL) due to the millimetric W ionisation length within SOL. This allows to disregard the line-of-sight (LoS) integration effect through the plasma volume as no neutral W sources exist there. In combination with the typical centimetric size of the target surface monitored by a LoS, this also allows one to consider that the magnetic field, and thus also its angle with respect to the LoS direction, are constant over the emission zone. The use of a Monte Carlo method for this model gives a lot of freedom regarding changes of the various parameters, and choices of different scenarios.

The input variables for the model are the background plasma parameters n_e, T_e, T_i, detector geometry (the angle of the detector with respect to the surface and the distance between them), source dimensions, incident species and their charge.

2.1. Incident particles

Under tokamak conditions various impurities are generally present, depending of the wall materials and seeded species. Therefore, in this work we use O as a representative impurity, which will always be present to some extent. When applying our results to a particular experiment, this assumption could be refined on the basis of measured impurity concentrations. For instance, in ITER, one would expect beryllium to play a significant role while in a full W machine O could be responsible for the bulk of the erosion. The determination of the dominant ionisation stages of oxygen is substantially more complicated. This would require a combination of spectroscopic investigation and plasma edge modeling to estimate the concentrations of differently charged oxygen at the SOL. Note that self sputtering by W ions is yet another particular case which can be treated with the model, depending on the situation.

The incident ion flux is assumed to be thermalised and to have a Maxwellian energy distribution, shifted by the sound speed in the parallel direction at the entrance of the sheath. At the sheath entrance the ion and electron temperatures are assumed to be equal $T_i = T_e$. It should be noted here that while the ion temperature is often not measured, it has been experimentally observed that T_i can be several times higher than T_e [13, 14], especially in the far scrape-off layer (SOL). The influence of the T_i/T_e ratio on the generated results is thus analyzed in Section 3.

This incident ion flux is considered to be accelerated in the sheath (Fig. 1, step 1), and the typical incident ion energy can be expressed as [15]:

$$E_{im} = 2T_i + 3T_e Z \tag{1}$$

Here Z is the ion charge. In most experimental cases the ion flux composition onto the plasma facing components is not measured. As these are expected to play a role in the W I line shape, the mass and charge of the incident ions are considered to be free parameters in our model.

2.2. Sputtering

All the sputtered particles in the model are generated by physical sputtering (Fig. 1, step 2). The sputtering yield is considered to follow the revised Bohdansky equation [16] and its dependence on the particle incidence angle is taken into account. However, the target is considered to be a completely smooth W surface.

The sputtered particles have a Thompson energy distribution [17, 18]:

$$P(E_{em}) = 2E_b \cdot \frac{E_{em}}{(E_{em} + E_b)} \cdot \frac{(E_i/E_{thr})^2}{(E_i/E_{thr} - 1)^2}. \tag{2}$$

Here $E_b = 8.68$ eV is the binding energy for W atoms, while E_{em} is the energy of the emitted particles and E_i is the energy of the incident ions. E_{thr} (threshold energy) is the minimum energy that an ion must transfer to the target atom to extract it from the surface and defines the distribution peak position. The emitted particles have a maximum possible emission energy which is proportional to the incident particle energy and can be expressed as (for $E_i > E_{thr}$):

$$E_{max} = E_b \cdot \left(\frac{E_i}{E_{thr}} - 1 \right) \tag{3}$$

The Thompson energy distribution for W sputtering at three different oxygen ion impact energies is presented in Figure. 2.

2.3. Emission

The energy distribution of the sputtered particles is a combination of the Thompson distribution and the Maxwellian distribution of the incident particles. The resulting distribution is presented in Figure 3 and shows features of both distributions: a steep

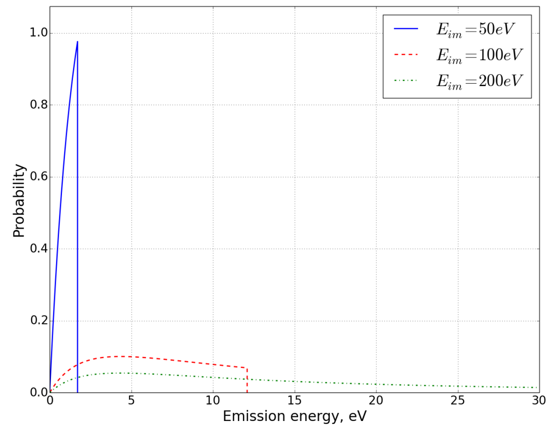

Figure 2. Thompson energy distribution for W sputtering at 3 different oxygen ion impact energies.

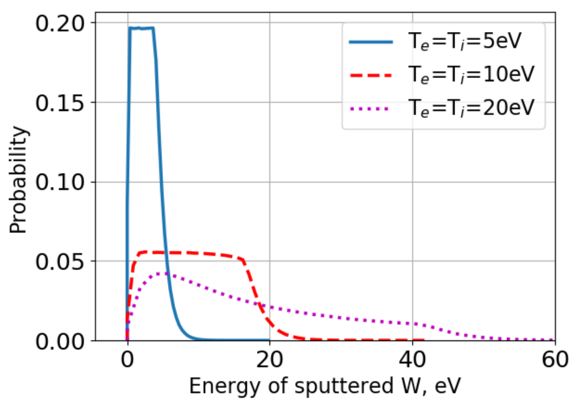

Figure 3. Sputtered particle energies, accounting for the energy distribution of impinging ions.

rise at low energy from the Thompson distribution and a continuous tail (in contrast to the sharp cut off seen in Figure 2). The values of $T_e = 5$, 10 and 20 eV were chosen as possible temperatures near the tokamak wall during normal operation [17, 19, 20]. Temperatures below $T_e = 5$ eV are not considered since the sputtering yield becomes very low at these conditions.

The combination of the Maxwellian distribution of incident particle energy and the Thompson energy distribution of sputtered particles can generate distribution functions with relatively wide flat top areas. This effect is more noticeable for simulations at low temperatures (T_i, T_e), where the cut-off of the Thompson distribution is located close to its peak.

Photon emission occurs randomly along the trajectory of sputtered atoms and within the W ionisation length (Fig. 1, steps 4 and 5). In order to reduce the computational time we consider that all the sputtered particles will get excited and undergo spontaneous decay in our specified spectral line, since the average number of excitation per ionization event is independent on the direction in which the atom is emitted. This is equivalent to setting the S/XB factor to 1. Absolute line intensities can be obtained either by using the measured S/XB value or by implementing the excitation process in the Monte Carlo process, which gives the same results if the atomic data are consistent.

It should be noted here that the model additionally relies on the facts I) that volume recombination of W^+ is negligible in the conditions where sputtering does occur and II) that the line considered is optically thin (which can be checked using e.g. Eq. (3) in Ref. [21], assuming that the population of the lower state of the transition is equal to the total W density, which is a conservative assumption). Furthermore, we assume there are no charge exchange processes involving neutral W. To our knowledge, there are no data available in the literature on such processes.

2.4. Angular dependence

The angular distribution of the sputtered particles must also be taken into account. When incident particle energies are above 500 eV the angular distribution of the sputtered particles is a cosine distribution. This impact energy of 500 eV would correspond to plasma temperatures of 35 eV for particles with a charge $Z = 4$. However, when the impact energy is less than 500 eV, the emitted particles have a more complex angular distribution. The latter is plotted in Figure 4, for W erosion by O^+ ions. This is the situation expected during the inter-ELM phases in H-mode operation, with plasma temperatures close to the divertor targets below 30 eV and down to a few eV's. At these temperatures, W sputtering is dominated by impurities for which the energy transfer to heavy W atoms in the lattice is more favorable. Table 1 shows impact energies of oxygen ions of increasing charge as a function of plasma temperatures, and indicates the corresponding range of sputtering yields. With increasing charge, the sheath acceleration becomes larger and fully determines the impact energy when $3ZT_\mathrm{e} \gg 2T_\mathrm{i}$. Also, note that W self sputtering threshold for singly ionized ions becomes significant at plasma edge temperatures of 10 eV [22]. It is thus fully relevant to discuss the angular distribution for low energy regime, i.e. $E_\mathrm{i} < 500$ eV, because significant sputtering also occurs in this regime.

It has been reported consistently in various sources that in this energy range the emitted particles have a butterfly-like spatial distribution [23, 24, 25]. This has to be taken into account in this study, as it will affect the velocity distribution function of W atoms along the observation direction. Assuming we have a detector looking along the normal to the surface, there will be a smaller number of emitted particles with velocity pointing towards the detector compared to a cosine distribution (because of the empty range in between the butterfly lobes). The particles with emission angles within the

Table 1. Energies (in eV) of incident oxygen ions with different charges after their acceleration in the plasma sheath. Different shaded cells: sputtering yield above 10^{-4} at/ion and 10^{-2} at/ion

T_i, eV	T_e, eV	O^+	O^{2+}	O^{3+}	O^{4+}	O^{5+}	O^{6+}	O^{7+}	O^{8+}
1	1	5	8	11	14	17	20	23	26
2	2	10	16	22	28	34	40	46	52
3	3	15	24	33	42	51	60	69	78
5	5	25	40	55	70	85	100	115	130
10	10	50	80	110	140	170	200	230	260
6	2	18	24	30	36	42	48	54	60
9	3	27	36	45	54	63	72	81	90
15	5	45	60	75	90	105	120	135	150

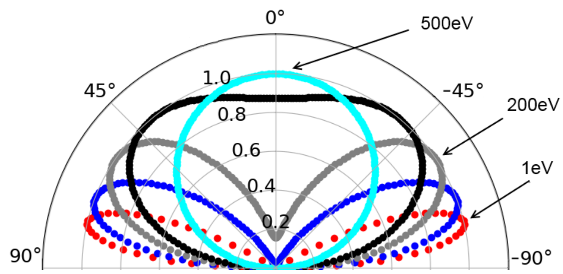

Figure 4. Angular distribution of sputtered W particles in polar coordinates for various incident particle energies

butterfly lobes would have smaller velocity projections towards the line of sight and would generate photons with a smaller blue shift. Note that the situation would be different in another observation direction.

Such a distribution can be represented as [26]:

$$f(x) = A\cos^n(\theta) + B\cos^m(\theta) \tag{4}$$

The exponent n increases with increasing atomic number and varies depending on the target material and incident species. The proposed estimation for the value of n is:

$$n = 0.3\left(\frac{Z}{E_b}\right)^{0.5}\left(1+\left(\frac{M_1}{2M_2}\right)^3\right) \tag{5}$$

where Z is the atomic number of the target material, E_b the binding energy in eV, M_1 and M_2 masses for bombarding (M_1) and target (M_2) atoms. As the remaining parameters (A, B and m) were not given explicitly by the authors, we have fitted them on the angular distributions provided by the authors [23, 24, 25]. The polynomial fits obtained agree well with the experimental and numerical results reported by several sources [23, 25, 26, 27].

Such an angular distribution arises because at low energies sputtering is considered to behave in the "knock off" manner. In this case all the collisions are considered

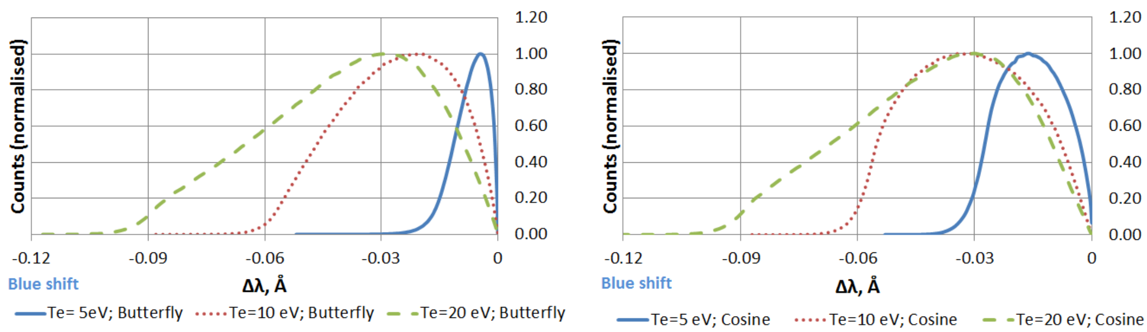

Figure 5. Simulated line-shape with different sputtered particle angular distribution at various plasma temperatures ($T_e = T_i$, sputtering by O^{4+} ions)

to happen only at the few topmost surface layers. Following the minimum energy-loss process these particles have a preferential angular distribution which is analysed in more detail in [27, 28].

For incident particle energies above 500 eV and up to the ˜10 keV range (e.g. during ELMs) the impact atoms can transfer enough energy to a target atom to displace other atoms within the target. This can be considered as a linear cascade of collisions. In such a case the angular distribution is close to a cosine law.

For example, the maximum incident particle energy during a type I ELM event is considered to be proportional to the electron pedestal temperature and equal to $E_{\text{impact,max}} = 4.23 \cdot T_{\text{e,max}}^{\text{ped}}$ [29]. In the ITER case the estimated $T_{\text{e,max}}^{\text{ped}}$ is about 5 keV, which means $E_{\text{impact,max}} \approx 20$ keV. The corresponding angular distribution of the sputtered atoms is thus well described by a cosine law.

On the contrary, during the inter-ELM phase in JET experiments the recorded T_e by Langmuir probes did not exceed 30 eV [29]. Assuming $T_e = T_i$ and $Z = 1$ would result in impact energies of $E_{\text{impact,max}} \approx 150$ eV. This indicates that in such a scenario even considering $Z = 3$ the angular distribution of the sputtered particles should still be considered non-cosine.

These geometrical considerations for the sputtered particle angles should contribute to the changes of the spectral line during inter- and intra-ELM phases of tokamak operation, on top of the effects resulting from very different incident energies. These two effects can either reinforce each other or partially cancel each other depending on the conditions and the observation direction.

The simulated lineshapes at identical plasma parameters but with different sputtered atom angular distributions are presented in Figure 5, assuming normal observation. It shows that while the angular distribution of sputtered particles does influence the expected line shape, the change is only significant at low temperature plasma conditions (inter-ELM phase). In these conditions ($T_e = T_i = 5$ eV) the FWHM of the predicted line shape reduces from 0.024 Å to 0.01 Å when considering a butterfly angular distribution for sputtered particles. This is in line with simple considerations on the projection of velocities on the observation direction.

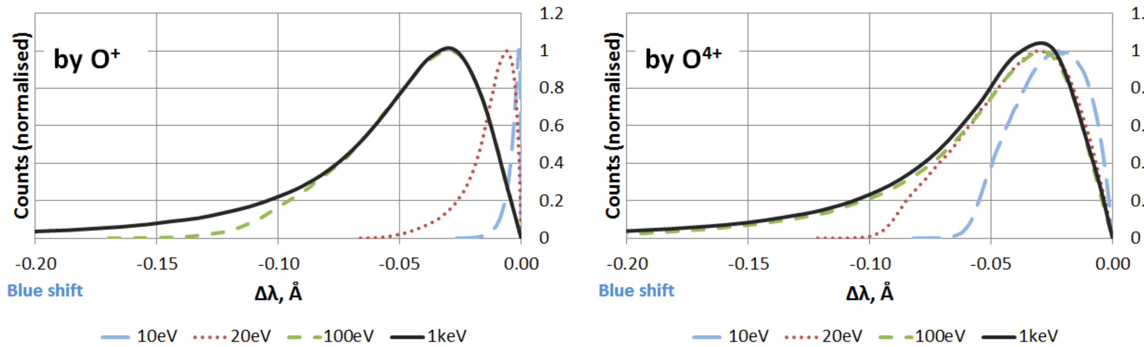

Figure 6. Calculated line shape for normal detector placement when sputtering is generated by O^+ and O^{4+} ions at various plasma temperatures $T_e = T_i$

At $T_e = 10$ eV the line shape still exhibits a dependence on the type of angular distribution but both the peak position and the line width remain practically unchanged. The profiles become almost identical at higher plasma temperatures as incident particles have higher energies and the angular distribution becomes more cosine-like shaped. Finally, it should be noted that this comparison assumes that the material surface is flat, so that the normal to the surface is identical on the whole spatial extension from which W atoms originate. In reality the surfaces have some level of roughness, which will contribute to blur the differences between cosine and butterfly distributions. However, at low energies the lobes of the butterfly distributions are quite narrow and it would take large fluctuations of the surface normal to make the effect irrelevant.

3. Results

Simulations were performed with different plasma temperatures, detector orientations and different incident species and charges, both in the inter- and intra-ELM phases. The Zeeman effect is dealt with in the subsequent section.

3.1. Normal detector

The predicted line shape for the most commonly observed W I line so far at 400.9 nm is presented in Figure 6. Here the x axis represents the wavelength difference with respect to the unshifted line position (0 being the unshifted 400.9 nm wavelength). Note that for the Doppler profile, only the wavelength scale is specific to this line – the shape would be identical for other lines. The results show that the spectral line should be entirely blue shifted due to the geometry of the simulation (red shifted photons would be emitted by sputtered particles with velocities away from the detector therefore directed back into the material). The width of the line also increases as expected with increasing plasma temperature and is in the range of $10^{-1} - 10^{-2}$ Å while the peak shift is of the order of 10^{-2} Å. For comparison, the typical thermal Doppler broadening for $kT \sim E_B \sim 10$ eV is indeed of the order of $3 \cdot 10^{-2}$ Å ($\frac{\Delta\lambda}{\lambda} = \sqrt{\frac{kT}{mc^2}}$). These values are small compared to the common spectral resolution of the typical tokamak spectrometers and indicates that the linewidth changes should be less challenging to resolve than the peak position shift.

It is evident from the simulated line shape that it depends on the plasma temperature and type of incident ion, showing noticeable differences between sputtering by O^+ and O^{4+} except for the high temperature cases, for which the distribution tends towards a limit distribution. When the ion charge increases keeping plasma parameters identical, the sheath acceleration $3ZT_e$ increases, and thus the impinging ion energy increases. This shift of energy range is clearly evidenced on Fig. 6: for the low Z sputtering case, corresponding to lower impact energies, the general line shape is quite asymmetric at all temperature conditions: a steep rise on the red side of the peak and a long decaying tail on the blue side. However, for the same plasma conditions but with $Z = 4$, the line shape approaches the (projected) Thompson distribution (Eq. 2) for lower temperatures. The peak position becomes essentially insensitive to the incident particle energy, and only the tail of the line shapes gets longer with increasing energy, an effect difficult to evidence experimentally. This is most evident when comparing the 100 eV and 1 keV cases. This analysis shows that while at high impact energies the line shape is largely insensitive to the exact plasmas conditions, it does provides a direct check on the energy distribution of sputtered particles.

3.2. Tilted detector

Subsequently, simulations were performed with the detector at an angle with respect to the surface. This allows one to mimic common experimental situations where the line of sight is tilted with respect to the surface normal, and investigate to what extent measuring the line shape along two line of sights with different inclinations would provide a check on the angular distribution of emitted atoms. Throughout this section the line of sight was placed at 60° to the surface normal. For comparison the simulations were performed with cosine and butterfly angular distributions of the emitted particles. The line shapes obtained with such configurations at various plasma conditions are presented in Figure 7.

As expected, the red wing of the spectral line appears when the line of sight is at an angle. This arises due to the fact that in tilted configurations it is possible for the particles to have velocity projections directed away from the detector.

Additionally, it is evident that accounting for the butterfly angular distribution for sputtered particles produces wider and more asymmetrical peaks. The strong asymmetry at low plasma temperatures results from the superposition of two distributions with different widths, one being blue-shifted and emitted by the lobe aligned with the observation direction and the other being red-shifted and emitted by the other lobe. The latter is narrower due to the asymmetry of the two lobes with respect to the observation direction. With increasing incident particle energy, the width of the red shifted component decreases as the angular distribution becomes more cosine-

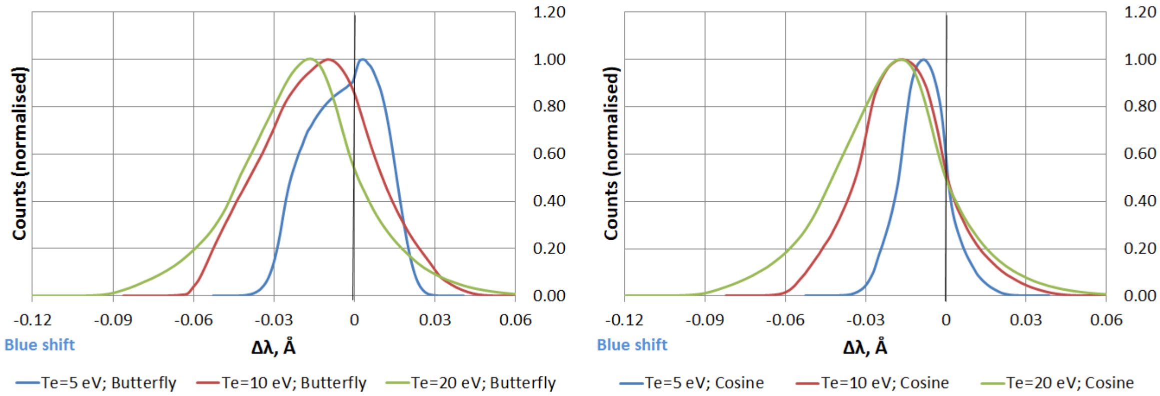

Figure 7. Simulated line shape for detector placement at a 60° angle to the surface normal at various plasma conditions ($T_e = T_i$, sputtering by O^{4+} ions, with different sputtered particle angular distributions)

like and the maximum achievable red shift becomes smaller. This FWHM (Full Width at Half Maximum) increase could slightly reduce the difficulty of resolving such spectral lines. This analysis clearly shows that simultaneous observations along two different directions would provide information on the angular distribution of emitted atoms.

3.3. Inter-ELM phase

During normal tokamak operation the temperature at the plasma edge has to be as low as possible to minimise the physical erosion and the related plasma contamination and plasma facing component damage. As this is the desired operational regime, the simulations for temperatures relevant for divertor operation in the inter-ELM phases were performed at low temperature values. They are presented in Figure 8. where sputtering was assumed to be only by O^{4+} ions. As the sputtering yield becomes smaller at lower particle energies, the results are normalised so the maximum of the distribution is 1, to better illustrate the change in the line shape.

The results reinforce the previous conclusion that the line shape is sensitive to the ion impact energy and that the line shape width changes might be more clearly visible than the peak shift itself. However such changes would be measurable only with a very high resolution spectrometer, tracking for instance the position of the line centroid and width during a divertor temperature scan. Performing such a line shape measurement in these inter-ELM/low temperature conditions is challenging, and would require a spectrometer with resolving power $\lambda/\Delta\lambda$ of approximately 400000, to resolve spectral features of 10^{-2} Å needed for the $T_e = 5$ eV case. In other words, we assume that the FWHM of the apparatus function should not be larger than the line shape width in order to be able to retrieve information. This also gives an indication about the shifts which would be measurable. At even lower temperatures the peak shift is of the order of 10^{-3} Å, but sputtering is then weak and the possibility to measure the line with a reasonable signal-to-noise ratio comes into question.

Spectrometers routinely used in tokamak plasma spectroscopy are, to the best of our knowledge, not able to provide the required spectral resolution (common Czerny-Turner spectrometers can for instance provide a maximum spectral resolution of about 0.02 Å, while the width of the spectral line at $T_e = 2$ eV conditions is of the order of 0.001 Å). However, it is possible to achieve larger spectral resolution (up to $R = 10^7$ according to manufacturers) with for example Littrow configuration spectrometers. Littrow configuration spectrometers can reach very high spectral resolutions, but operate with very small apertures. Another possibility would be to use a scanning Fabry-Perot interferometer with appropriate filters. Such instruments have been long used to analyse astronomical plasmas [30], and recently attempts to measure ion temperature by the use of interferometry in weakly magnetized plasmas were performed [31]. More recent developments are combining the advantages of Fabry-Perot cavities with those of grating spectrometers, making use of virtually-imaged phased array (VIPA) [32], with compact $R = 10^6$ spectrometers commercially available. Such measurements might in any case require optimising the throughput of the system and using long acquisition times (possibly making use of long steady state discharges in tokamaks such as WEST [3] or EAST), accumulating data only in between - or during - the ELMs.

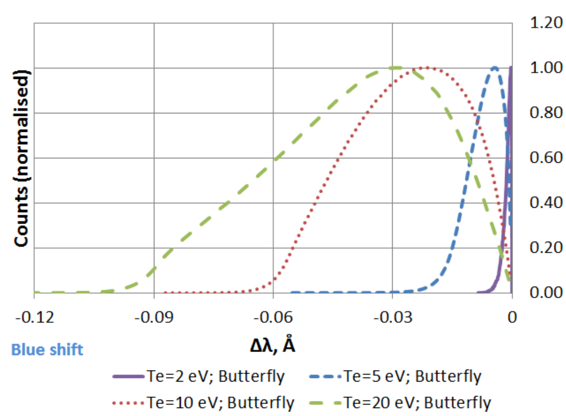

Figure 8. Predicted line shape for low temperature plasma conditions, when sputtering by O^{4+} ions

3.4. Intra-ELM phase

It is known that T_e is very low during the ELM events ($\approx 20 - 30$ eV or less [29]). Since the typical incident ion energy is $2T_i + 3T_eZ$ and $T_i \gg T_e$, the analysis of the spectral line shape could yield indirect measurements of the plasma ion temperature T_i.

The calculated line shape for plasma temperatures relevant to the intra-ELM phase is presented in Figure 9. In this case it is assumed that $T_e = T_i = 1$ keV. Since our previous argument states that the influence of T_e can be neglected, it can be considered that the presented lines correspond to T_i values of 2.5 keV for O^+ and D^+ and 7 keV for O^{4+}. It is evident that at high temperatures the line shape does not depend on the

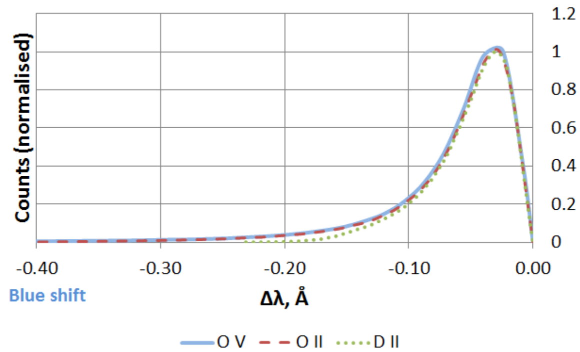

Figure 9. Calculated line shape when sputtering by O^{4+} (O V), O^{+} (O II) and D^{+} (D II) ions at $T_{\mathrm{e}} = T_{\mathrm{i}} = 1$ keV

temperature and only the tail broadens (because the cut-off energy of the Thompson distribution increases with the incident particle energy). In fact, from previous results it is evident that the line width varies insignificantly with plasma temperatures above 100 eV (Figure 6). While this shows that it is not possible to infer T_{i} during the ELM event from the line shape, it should make the profile measured during ELMs markedly different from that obtained in the inter-ELM phase. This is a good check on the sensitivity of the diagnostic, but also on the underlying assumptions of the model, by providing direct access to the energy distribution of sputtered atoms on a wide energy range (which is not possible at lower energies, for obvious energy conservation reasons).

3.5. Sensitivity to T_{i}

The initial assumption $T_{\mathrm{e}} = T_{\mathrm{i}}$ at the sheath entrance may often underestimate the value of T_{i}, for which measurements are rather scarce. As mentioned earlier T_{i} is often observed to be several times higher than T_{e}, especially in the region far from the separatrix [13]. This can lead to significant sputtering even rather far from the separatrix. The comparison between the line shapes estimated by our model considering $T_{\mathrm{i}} = T_{\mathrm{e}}$ and $T_{\mathrm{i}} = 3T_{\mathrm{e}}$ are presented in Figure 10. This result shows that as soon as the electron temperature is larger than a few eV, the increase in T_{i} does not change the results significantly since we already are in the high impact energy regime (above 100 eV), where only the tail of the Doppler line shape is affected. In fact, for the conditions shown on Figure 10, we have impact energies of the order of 150 eV.

At lower impact energies, the effect of the $T_{\mathrm{i}}/T_{\mathrm{e}}$ ratio is expected to be stronger, since it contributes in determining the impact energy. However, as mentioned earlier, ions reaching the surface are considered to have an energy distribution with mean energy $E = 2T_{\mathrm{i}} + 3T_{\mathrm{e}}Z$. One can rewrite this energy as $E = T_{\mathrm{e}}(\frac{2T_{\mathrm{i}}}{T_{\mathrm{e}}} + 3Z)$, which shows that T_{i} controls the incident energy only when $Z \ll \frac{2}{3}\frac{T_{\mathrm{i}}}{T_{\mathrm{e}}}$. This leads to the condition $Z \ll \frac{2}{3}\frac{T_{\mathrm{i}}}{T_{\mathrm{e}}} \approx 2$ if we assume that $\frac{T_{\mathrm{i}}}{T_{\mathrm{e}}} = 3$. It shows that as soon as $Z \geq 2$, the incident particle energy is defined by the incident ion charge rather than by the T_{i} value at the

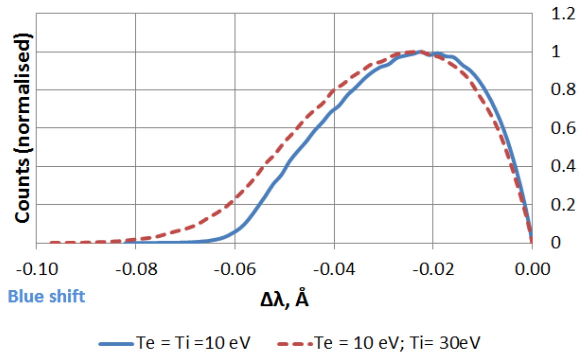

Figure 10. Calculated line shape assuming different T_i/T_e ratios, for O^{4+} incident ions.

sheath entrance.

4. Zeeman effect

It is well known that in tokamak environment the spectral lines exhibit a Zeeman splitting due to the presence of a magnetic field. Since the aim of this study is to investigate the possibility of inferring plasma parameters from the spectral line shape, this effect can not be overlooked.

To the best of our knowledge, as of this date there is no reported in-depth analysis of the $5d^5(^6S)6s\ ^7S_3$ - $5d^5(^6S)6p\ ^7P^0_4$ W I 400.9 nm spectral line Zeeman splitting, even though Zeeman patterns have been published [6, 12]. We provide in the Appendix the calculation of the positions and relative intensities of the Zeeman components for this line. An example of the resulting Zeeman pattern is shown in Figure 11. Here the Zeeman structure is well resolved and despite some overlapping of the central and lateral components the typical triplet shape starts to appear. The validity of the weak field approximation is marginal for this field strength ($B = 2.5$ T) but treating the case where fine structure is of the same order (Paschen-Back effect) or negligible compared to the Zeeman splitting (strong field) requires more information about the states involved than just the spectroscopic terms, and this is outside the scope of the current work.

The convolution of the Zeeman profile (at $B = 2.5$ T and with a line of sight perpendicular to the direction of the B field ($\theta = 90°$)) with the calculated Doppler line is shown in Figure 11. Since the width of the modelled line is lower than the gap between the Zeeman components the Zeeman profile can be clearly seen. However, in the higher plasma temperature cases ($T_e = T_i > 5$ eV) the modelled line shape width becomes wider than the spacing between the individual Zeeman components and the contributions from the different components start to overlap. The expected line-shape in such a case is presented in Figure 12. The magnetic field strength at the magnetic axis of the ITER plasmas is expected to be above 5 T. A similar magnetic field is expected on the ITER plasma divertor legs. In such a case the Zeeman splitting should be wider

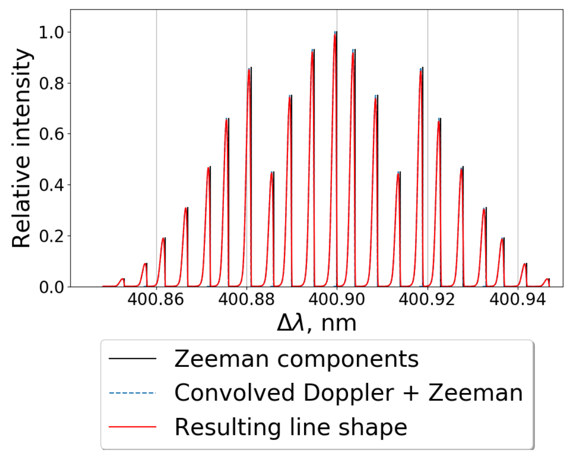

Figure 11. Convolved Zeeman - Doppler lineshape, at $T_\mathrm{e} = T_\mathrm{i} = 5$ eV, for $Z = 4$, $\theta = 90°$ and $B = 2.5$ T

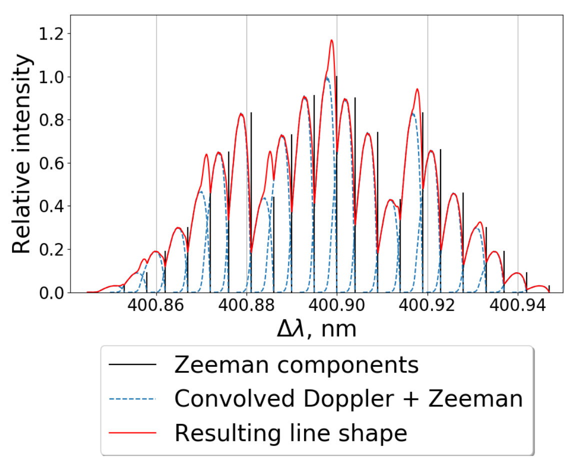

Figure 12. Convolved Zeeman - Doppler lineshape, at $T_\mathrm{e} = T_\mathrm{i} = 10$ eV, for Z = 4, $\theta = 90°$ and $B = 2.5$ T

than proposed in this study and such overlapping should be minimal (but the weak field approximation used here is no longer valid).

As a final point, we discuss the question of the natural width of the line. The latter can be calculated from the value of the Einstein coefficient for the transition, namely $A_{ki} = 1.63 \times 10^7$ s^{-1} [33] for the line under discussion. The full width at half maximum (FWHM) of the Lorentzian resulting from the natural broadening of the line is then given (in angular frequency) by

$$\Delta\omega = A_{ki} \tag{6}$$

This gives the following value for the FWHM in wavelength,

$$\Delta\lambda = \frac{\lambda_0^2}{2\pi c}\Delta\omega \simeq 1.4 \times 10^{-5} \mathring{A} \tag{7}$$

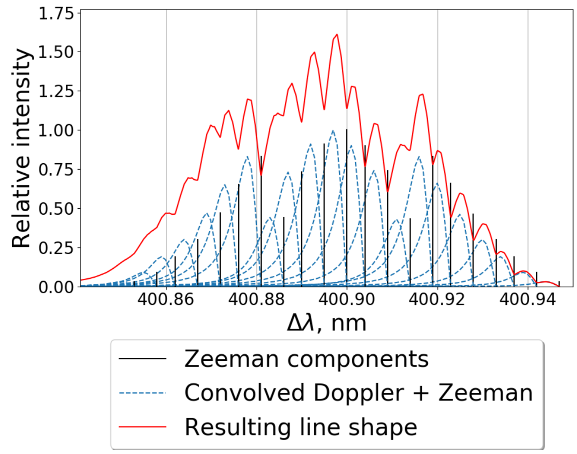

Figure 13. Convolved Zeeman - Doppler lineshape, at $T_e = T_i = 1$ keV, for $Z = 4$, $\theta = 90°$ and $B = 2.5T$

where λ_0 is the wavelength of the line center, and c the speed of light. This rough calculation (neglecting the fact that the line is split in several components) shows that the natural width is small enough to be ignored in our analysis.

5. Summary

A Monte Carlo model for simulating the W I spectral line shape was developed. The parameters controlling the line shape of the W I spectral line have been investigated, and the possibility to extract information on these parameters from a line shape analysis has been discussed. The results also apply to other W I lines, except for the Zeeman effect which is line specific. The simulations show that the modelled Doppler line shape depends on the ion impact energy (itself a function of T_e, T_i and the charge of the incident particles). For impact energies above ~ 100 eV, the line shape essentially converges to the Thompson distribution projected on the observation direction, and thus provides a check on the model assumptions instead of information on the plasma conditions. This is relevant for the intra-ELM phase, while during the inter-ELM phase a line shape analysis would help characterizing ion impact energies, and thus plasma conditions in conjunction with other diagnostics, such as probe measurements for T_e, Z_{eff}... The angular distribution of the sputtered atoms plays an important role in the analysis of the Doppler profiles, and simultaneous measurements at different viewing angles are shown to provide strong checks on model assumptions.

In the inter-ELM phase the predicted Doppler peak shift for the 4009 Å line is of the order of 10^{-2} Å. For the higher wavelengths this result is expected to be slightly higher due to the linear dependence between the shift and the central wavelength of the line. While the Doppler shift is likely to be difficult to resolve, the line shape changes are shown to be measurable using appropriate commercially available high resolution spectrometers. Such measurements are likely to require averaging over a long acquisition time, the limits being set by the duration of achievable stationary phases in discharges, and proper optimization of the optical throughput of the system. During the intra-ELM phase the predicted line shape practically does not depend on the incident particle energy. According to our model, Doppler profiles should differ significantly during and in between ELMs, which could provide a simple check on the ability to resolve the profile.

Interpretation of the Doppler line shape is likely to require an accurate Zeeman pattern model when the Doppler shift is comparable to the magnetic field and/or the fine structure splitting of the line, so that merging of different components is observed. The measurements of the lineshape should include several W I lines in order to verify whether line shape changes are consistent with Zeeman pattern calculations, and allow identifying possible parasitic line contributions. Additionally, the measurement of several spectral lines simultaneously would help choosing the optimal spectral line in terms of sensitivity and Zeeman pattern - the commonly used 400.9 nm line does have a complex Zeeman structure, while some others will have more triplet like features for instance, which could facilitate the analysis.

Acknowledgments

Discussions with Olivier Peyrusse are gratefully acknowledged. This work has been carried out within the framework of the EUROfusion Consortium and French Research Federation for Fusion Studies and has received funding from the Euratom research and training programme 2014-2018 and 2019-2020 under grant agreement No 633053. The views and opinions expressed herein do not necessarily reflect those of the European Commission.

Appendix: Zeeman pattern for the $5d^5(^6S)6s\ ^7S_3$ - $5d^5(^6S)6p\ ^7P^0_4$ transition at 400.9nm

In the following, we calculate the Zeeman pattern of the $5d^5(^6S)6s\ ^7S_3$ - $5d^5(^6S)6p\ ^7P^0_4$ transition in the weak field approximation, namely when the Zeeman splitting is small compared to the fine structure splitting, as is the case here (the other lines of the multiplet are respectively at 407.43 nm and 428.46 nm). Here θ is the angle between the magnetic field and the observation direction, defined by a unit vector $\mathbf{k}$. The intensity of the line can be written as

$$I(\omega, \mathbf{k}) = \sum_{\alpha\beta} |\langle\alpha|\mathbf{d}\cdot\boldsymbol{\epsilon}_\perp|\beta\rangle|^2\, \delta\left(\omega - \omega_{\alpha\beta}\right) \tag{A.1}$$

where $|\alpha\rangle$ are the upper levels and $|\beta\rangle$ the lower levels of the transition, $\omega_{\alpha\beta} = (E_\alpha - E_\beta)/\hbar$ and δ is the Dirac delta function. Here the upper level has a total angular momentum number $J = 4$, and the lower level is such that $J = 3$. For a vanishing magnetic field, the magnetic sublevels are degenerate, with a degeneracy $2J+1$, corresponding to $|M_J| \leq J$. $\boldsymbol{\epsilon}_\perp$ is the polarization vector, which is in the plane perpendicular to the observation direction $\boldsymbol{k}$, and $\mathbf{d}$ is the electric dipole operator. The double sum on the upper and lower states is reduced to a single sum by the selection rule $\Delta M_J = 0, \pm 1$, yielding the following result for the intensity of the line

$$I = \frac{1}{2}\sin^2\theta \times I_\pi + \left(\frac{1}{4} + \frac{1}{4}\cos^2\theta\right) \times (I_{\sigma^+} + I_{\sigma^-}) \tag{A.2}$$

where I_π and $I_{\sigma\pm}$ correspond to different polarisations. Explicitly, we have

$$I_\pi(\Delta\omega) = \sum_{M_j=-3}^{3} C^\pi_{M_J} I_0\left(\Delta\omega + \frac{\omega_Z}{4}M_J\right) \tag{A.3}$$

$$I_{\sigma^\pm}(\Delta\omega) = \sum_{M_j=-3}^{3} C^\sigma_{M_J} I_0\left(\Delta\omega \pm \frac{\omega_Z}{4}(M_J - 7)\right), \tag{A.4}$$

where the Larmor frequency $\omega_Z = \frac{eB}{2m_e}$, $\Delta\omega = \omega - \omega_0$ with ω_0 the frequency of the unperturbed line, and the relative intensity of components, after evaluation of the relevant 3j-symbols for the transitions [34], is given by

$$C^\pi_{M_J} = \frac{16 - M_J^2}{84}, \tag{A.5}$$

$$C^\sigma_{M_J} = \frac{(M_J+4)(M_J+5)}{168}. \tag{A.6}$$

References

[1] A. Kallenbach et al. Overview of ASDEX upgrade results. *Nuclear Fusion*, 57(10):102015, Jun 2017.

[2] G.F. Matthews. Plasma operation with an all metal first-wall: Comparison of an ITER-like wall with a carbon wall in JET. *Journal of Nuclear Materials*, 438:S2–S10, 2013. Proceedings of the 20th International Conference on Plasma-Surface Interactions in Controlled Fusion Devices.

[3] J. Bucalossi, M. Missirlian, P. Moreau, F. Samaille, E. Tsitrone, D. van Houtte, T. Batal, C. Bourdelle, M. Chantant, Y. Corre, X. Courtois, L. Delpech, L. Doceul, D. Douai, H. Dougnac, F. Faisse, C. Fenzi, F. Ferlay, M. Firdaouss, L. Gargiulo, P. Garin, C. Gil, A. Grosman, D. Guilhem, J. Gunn, C. Hernandez, D. Keller, S. Larroque, F. Leroux, M. Lipa, P. Lotte, A. Martinez, O. Meyer, F. Micolon, P. Mollard, E. Nardon, R. Nouailletas, A. Pilia, M. Richou, S. Salasca, and J.-M. Travère. The WEST project: Testing ITER divertor high heat flux component technology in a steady state tokamak environment. *Fusion Engineering and Design*, 89(7):907–912, 2014. Proceedings of the 11th International Symposium on Fusion Nuclear Technology-11 (ISFNT-11) Barcelona, Spain, 15-20 September, 2013.

[4] D.E.T.F. Ashby and M.H. Hughes. A study of the effect of impurity radiation from the peripheral plasma of a tokamak reactor. *Nuclear Fusion*, 21(8):911–926, Aug 1981.

[5] V Philipps, R Neu, J Rapp, U Samm, M Tokar, T Tanabe, and M Rubel. Comparison of tokamak behaviour with tungsten and low-Z plasma facing materials. *Plasma Physics and Controlled Fusion*, 42(12B):B293–B310, Dec 2000.

[6] S Brezinsek, M Laengner, J W Coenen, M G O'Mullane, A Pospieszczyk, G Sergienko, and U Samm. Spectroscopic determination of inverse photon efficiencies of W atoms in the scrape-off layer of TEXTOR. *Physica Scripta*, T170:014052, Oct 2017.

[7] N. Den Harder, S. Brezinsek, T. Pütterich, N. Fedorczak, G.F. Matthews, A. Meigs, M.F. Stamp, M.C.M. van de Sanden, and G.J. Van Rooij. ELM-resolved divertor erosion in the JET ITER-like wall. *Nuclear Fusion*, 56(2):026014, Jan 2016.

[8] Hans R. Griem. *Principles of Plasma Spectroscopy*. Cambridge Monographs on Plasma Physics. Cambridge University Press, 1997.

[9] E. Stambulchik, A. Calisti, H.-K. Chung, and M. Á. González. Spectral Line Shapes in Plasmas II. *Atoms*, 7(1):20, 2019.

[10] J. Rosato, N. Kieu, M. Meireni, R. Sheeba, M. Koubiti, Y. Marandet, R. Stamm, K. Verhaegh, B. Duval, The TCV team, and The MST1 team. Stark broadening of Balmer lines with low and moderate quantum number in dense divertor plasmas. *Contributions to Plasma Physics*, 58(6–8):578–582, 2018.

[11] R Guirlet, M Koubiti, A Escarguel, C De Michelis, M Mattioli, M O'Mullane, H Capes, L Godbert-Mouret, and R Stamm. Experimental and theoretical evaluation of the He II 6560.1 å line contribution to the deuterium Dα spectral line shape in Tore Supra ergodic divertor plasmas. *Plasma Physics and Controlled Fusion*, 43(2):177–194, Jan 2001.

[12] I Beigman, A Pospieszczyk, G Sergienko, I Yu Tolstikhina, and L Vainshtein. Tungsten spectroscopy for the measurement of W-fluxes from plasma facing components. *Plasma Physics and Controlled Fusion*, 49(11):1833–1847, Oct 2007.

[13] M Kocan, J. P Gunn, J-Y Pascal, G Bonhomme, C Fenzi, E Gauthier, and J-L Segui. Edge ion-to-electron temperature ratio in the Tore Supra tokamak. *Plasma Phys. Control. Fusion*, 50(12):125009, Dec 2008.

[14] A Huber, A Pospieszczyk, B Unterberg, M Brix, Ph Mertens, Philipps V., and B Schweer. Spectroscopic measurements of the ion temperature profile in front of a limiter in TEXTOR-94. *Plasma Physics and Controlled Fusion*, 42:569, May 2000.

[15] A. Kirschner, D. Matveev, D. Borodin, M. Airila, S. Brezinsek, M. Groth, S. Wiesen, A. Widdowson, J. Beal, H.G. Esser, J. Likonen, N. Bekris, and R. Ding. Modelling of the material transport and layer formation in the divertor of JET: Comparison of ITER-like wall with full carbon wall conditions. *Journal of Nuclear Materials*, 463:116–122, 2015. Plasma Surface Interactions 21.

[16] C. Garcia-Rosales, W. Eckstein, and J. Roth. Revised formulae for sputtering data. *Journal of Nuclear Materials*, 218(1):8–17, 1995.

[17] *Atomic and Plasma Material Interaction Data for Fusion*. Number 12 in Atomic and Plasma Material Interaction Data for Fusion. International Atomic Energy Agency, Vienna, 2003.

[18] M. W. Thompson. The energy spectrum of ejected atoms during the high energy sputtering of gold. *The Philosophical Magazine: A Journal of Theoretical Experimental and Applied Physics*, 18(152):377–414, 1968.

[19] H J Sun, E Wolfrum, T Eich, B Kurzan, S Potzel, and U Stroth. Study of near scrape-off layer (SOL) temperature and density gradient lengths with Thomson scattering. *Plasma Physics and Controlled Fusion*, 57(12):125011, nov 2015.

[20] M.Z. Tokar and V. Kotov. Modelling the transport of deuterium and tritium neutral particles in a divertor plasma. *Nuclear Fusion*, 52(10):103004, Aug 2012.

[21] J. D. Hey. Optical spectroscopy of tokamak plasmas. *Transactions of fusion technology*, 25(2T):315–325, Mar 1994.

[22] W. Eckstein and J. László. Sputtering of tungsten and molybdenum. *Journal of Nuclear Materials*, 183(1):19–24, 1991.

[23] A. Eksaeva, E. Marenkov, D. Borodin, A. Kreter, M. Reinhart, A. Kirschner, J. Romazanov, A. Terra, S. Brezinsek, and K. Nordlund. ERO modelling of tungsten erosion in the linear plasma device PSI-2. *Nuclear Materials and Energy*, 12:253–260, 2017. Proceedings of the 22nd International Conference on Plasma Surface Interactions 2016, 22nd PSI.

[24] E. Marenkov, K. Nordlund, I. Sorokin, A. Eksaeva, K. Gutorov, J. Jussila, F. Granberg, and D. Borodin. Angular and velocity distributions of tungsten sputtered by low energy argon ions.

Journal of Nuclear Materials, 496:18–23, 2017.

[25] D. Nishijima, M.J. Baldwin, R.P. Doerner, and J.H. Yu. Sputtering properties of tungsten 'fuzzy' surfaces. *Journal of Nuclear Materials*, 415(1, Supplement):S96–S99, 2011. Proceedings of the 19th International Conference on Plasma-Surface Interactions in Controlled Fusion.

[26] Yu. V. Martynenko, A. V. Rogov, and V. I. Shul'ga. Angular distribution of atoms during the magnetron sputtering of polycrystalline targets. *Technical Physics*, 57(4):439–444, Apr 2012.

[27] Yasunori Yamamura, Yoshiyuki Mizuno, and Hidetoshi Kimura. Angular distributions of sputtered atoms for low-energy heavy ions, medium ions and light ions. *Nuclear Instruments and Methods in Physics Research Section B: Beam Interactions with Materials and Atoms*, 13(1):393–395, 1986.

[28] Y. Yamamura and J. Bohdansky. Few collisions approach for threshold sputtering. *Vacuum*, 35(12):561–571, 1985.

[29] C Guillemaut, A Jardin, J Horacek, I Borodkina, A Autricque, G Arnoux, J Boom, S Brezinsek, J W Coenen, E De La Luna, S Devaux, T Eich, D Harting, A Kirschner, B Lipschultz, G F Matthews, A Meigs, D Moulton, M O'Mullane, and M Stamp and. Experimental estimation of tungsten impurity sputtering due to type I ELMs in JET-ITER-like wall using pedestal electron cyclotron emission and target Langmuir probe measurements. *Physica Scripta*, T167:014005, Jan 2016.

[30] Benoit Epinat. *Des galaxies proches aux galaxies lointaines: études cinématique et dynamique.* PhD thesis, Université de Provence - Aix-Marseille, 2008.

[31] Victor Désangles. *Forçage à grande échelle d'une colonne de plasma faiblement magnétisée: influence d'une cathode émissive de grande taille.* PhD thesis, Ecole Normale Supérieure de Lyon, 2018.

[32] M. Shirasaki. Large angular dispersion by a virtually imaged phased array and its application to a wavelength demultiplexer. *Opt. Lett.*, 21(5):366–368, Mar 1996.

[33] A. Kramida, Yu. Ralchenko, J. Reader, and NIST ASD Team (2018). NIST Atomic Spectra Database (ver. 5.6.1), Available: `https://physics.nist.gov/asd` [2015, April 16]. National Institute of Standards and Technology, Gaithersburg, MD., 2018.

[34] Robert D Cowan. *The theory of atomic structure and spectra.* Univ of California Press, 1981.